High-pressure–high-temperature phase diagram of tin

Robin Fréville [○],[1] Agnès Dewaele [○],[1] Nicolas Guignot,[2] Philippe Faure,[3] Laura Henry,[1,2]
Gaston Garbarino,[4] and Mohamed Mezouar[4]

[1]*CEA, DAM, DIF, 91297 Arpajon, France and Université Paris-Saclay, CEA,
Laboratoire Matière en Conditions Extrêmes, 91680 Bruyères-le-Châtel, France*
[2]*Synchrotron Soleil, L'orme des merisiers, 91190 Saint-Aubin, France*
[3]*CEA, DAM, VALDUC, Is-sur-Tille 21120, France*
[4]*European Synchrotron Radiation Facility, BP220, 38043 Grenoble Cedex, France*

The high-pressure–high-temperature behavior of tin has been measured with x-ray diffraction and laser-heated diamond anvil cells up to 225 GPa at 300 K and to 110 GPa and ~4000 K. Temperature has been measured using conventional point pyrometry as well as a four-color mapping pyrometer. The stability fields of Sn liquid and solid phases (β-Sn, bct γ-Sn, bcc-Sn, hcp-Sn) have been constrained. The high-pressure hcp-Sn phase has been observed but at higher pressure than under hydrostatic compression. The bcc-bct transition conditions are measured, up to a bcc-bct-liquid triple point at 18.9 GPa/1410 K. A lower bound for bcc-Sn melting line is proposed (Simon equation): $T_m = 581((P - 2.86)/6.44 + 1)^{0.71}$ (P in GPa, T_m in Kelvin).

I. INTRODUCTION

Tin has an intermediate position between semiconducting (Si, Ge) and metallic (Pb) elements of the group 14. Pb has a relatively simple phase diagram [1], while semiconducting elements experience several phase transitions in pressure and temperature [2,3]. As an intermediate, Sn presents unusual bonding changes as a function of pressure and temperature. At ambient conditions, Sn is stable in its metallic β-Sn phase (space group: $I4_1/amd$). However, upon cooling below 286 K, Sn undergoes a phase transition to brittle α-Sn with a diamond structure [4] and a 27% volume expansion, a phenomenon known as a "tin pest." The compression behavior of Sn is well known below 20 GPa [5–8] and room temperature compression has been performed to 230 GPa [5,9–11], evidencing multiple phase changes.

Above 10.8 GPa, Sn transforms into a body-centered tetragonal structure (bct) γ-Sn (space group: $I4/mmm$) with an initial c/a ratio of ~0.91. Upon further compression, Salamat *et al.* [10] have evidenced a distortion from the bct structure to an orthorhombic one (bco, space group: $Immm$) with a small deviation between a and b ($a = 0.996 \times b$) at around 32 GPa. The bco phase then transforms sluggishly into a body-centered cubic (bcc) phase (space group: $Im\bar{3}m$) with a coexistence range of 30 GPa (from 40 to 70 GPa). The bcc-phase of tin remains stable up to ~150 GPa, where a bcc to hcp (hexagonal close packed, space group: $P6_3/mmc$) phase transition begins. Hcp-Sn was observed by static compression at 300 K [9,11]. One theoretical study predicts a return to the bcc phase above 1.3 TPa, and a bell shaped domain of stability for the hcp phase [12]. This could explain why this structure was not observed during ramp compression on tin, where the $P - T$ path are close to an isentrope [13].

Upon heating, the exact phase diagram of tin (melting curve and solid phases stability) remains debated [5,14,15]. A

review has been performed recently by Deffrennes *et al.* [15]. The melting curve was studied by shock compression up to 50 GPa [16,17] and with laser-heated diamond anvil cell using an optical detection of melting up to 68 GPa [18] and with a x-ray diffraction diagnostic up to 72 GPa [19,20]. Above this pressure, no x-ray diffraction experiments were carried out. Briggs *et al.* performed thermal analysis (increase in the laser power and observation of a plateau in temperature when the sample melted) up to 105 GPa to measure the extension of the melting curve beyond 72 GPa. The measured melting curve forms a plateau around 2700 K between 72 and 105 GPa [20].

We report here *in situ* measurements with x-ray diffraction (XRD) of laser-heated tin in diamond anvil cells, up to 110 GPa at 4000 K. Additionally, we have collected data at room temperature up to 20 GPa under hydrostatic compression, and up to ~230 GPa under nonhydrostatic compression. The stability of solid phases of tin is discussed, and new data are provided to constrain the melting curve of tin in the Mbar range.

II. EXPERIMENTAL PROCEDURES

A. Sample preparation

Two types of samples were used during our experiments: laminated tin foil (99.95% purity, Goodfellow) of 5 µm starting thickness and tin powder grains (99.8% purity, Alfa Aesar). The experimental conditions for each run are described in Table I.

For laser-heating runs (Sn33-Sn48), the starting samples were discs with diameters varying from 10 to ~70 µm, cut with a femtosecond laser coming either from the laminated foil or from powder grain crushed to form a ~2 µm thick platelet. All samples were loaded in a diamond-anvil cell (DAC) equipped with diamond culet size varying from 300

TABLE I. Experimental details. * mean that the starting sample was a grain powder crushed to form a disk. PP: point pyrometry; 4C: four color pyrometry (see text). Pressure transmitting medium (PTM) was also used as pressure marker in all runs except Sn30.

Run	Anvil culet (μm)	Sample	PTM/ P marker	Pyrometer	P range (GPa)	T range (K)	Beamline
Sn30	500	2 grains	He/Au	/	0–13	300–425	PSICHE
Sn33	300	one grain*	KCl/KCl	PP	0–45	300–2200	PSICHE
Sn34	70 × 300	one grain*	KCl/KCl	/	50–230	300	PSICHE
Sn35	300	one grain*	KCl/KCl	/	0–20	300	PSICHE
Sn37	70 × 300	foil	KI/KI	PP	5–65	300–2800	PSICHE
Sn39	100 × 300	foil	MgO/MgO	PP	27–115	300–2200	PSICHE
Sn42	150 × 350	foil	KI/KI	PP/4C	50–95	300–3000	PSICHE
Sn43	150 × 350	foil	KI/KI	PP/4C	90–110	300–4500	PSICHE
Sn46	100 × 300	foil	KI/KI	PP/4C	60–95	300–4200	PSICHE
Sn47	300	foil	KI/KI	PP	20–70	300–3500	ID27
Sn48	200 × 300	foil	KI/KI	PP	25–75	300–3300	ID27

to 70 μm in order to cover the 0–230 GPa pressure range, and a rhenium gasket. Each sample was loaded in the gasket hole between two platelets of a pressure transmitting medium (PTM), that also acted as a thermal insulator between the diamonds and the sample, and as pressure gauge. During pressure increase, the sample discs diameter increased, indicating a plastic strain enabled by the softness of tin. Sample thickness was thus less than 5 μm for all studied samples.

The high reflectivity of high-pressure Sn in the infrared range [21] renders laser-heating challenging for this metal, and we had to optimize the sample assembly design. First, to increase sample thermal insulation, KI was used as PTM in most runs because it has a smaller thermal conductivity than other alkali halides [22]. Second, an insulating Al_2O_3 treatment was used on several anvils. Third, Sn sample surfaces were depolished either with femtosecond laser patterning or by mechanical scratching of the surface, in order to decrease the reflection of heating laser, similarly to what has been previously done for another metal with a high reflectivity [23]. Our experience is that femtosecond laser patterning does not affect the bulk of the sample [24]. No chemical reaction could be detected from XRD spectra of samples with such surface treatment. The de-polishing survived after compression to high pressure as seen on samples pictures presented in Ref. [25]. To finish, for the highest pressure runs, cavities of 6 μm depth were drilled on the diamond anvil surface in order to increase the thickness of the pressure chamber and subsequent thermal insulation.

One experiment (run Sn30) was dedicated to the study of the $\beta - Sn \leftrightarrow$ bct-Sn transition under hydrostatic compression. The starting samples were two Sn powder grains, placed in the center of the experimental chamber with one Au powder grain to measure the pressure inside the chamber. They were loaded in helium to achieve hydrostatic pressurizing conditions [26,27] (see Ref. [25]).

B. XRD and laser-heating setups

Experiments were carried out at the PSICHE beamline of the SOLEIL synchrotron (France) and at the ID27 beamline of the European Synchrotron Radiation Facility (ESRF, France). Angular dispersive x-ray diffraction (XRD) data were

collected using an incident x-ray beam (wavelength = 0.3738 Å) of 8×12 μm^2 full width at half maximum (FWHM) spot on CdTe 2M PILATUS detector (PSICHE) and an incident x-ray beam of 0.8×0.8 μm^2 FWHM spot on an EIGER detector (ID27), both calibrated using a reference CeO_2 sample. The sample to detector distance was about ∼370 mm in both cases.

Pressure at 300 K was determined using the equations of state (EOS) of KCl [28], MgO [29], KI [22], and Au [30]. Since these gauges derived from ruby calibration [29], uncertainties in pressure is close to the uncertainty of ruby pressure scale: ±2.5 % at 150 GPa [31]. For KI, the pressure at high temperature was determined by adding a thermal pressure term to the EOS at 300 K:

$$P(V, T) = P(V, 300K) + \alpha K_T (T - 300),\qquad(1)$$

where the pressure P is in GPa, α the volumetric thermal expansion coefficient in K^{-1} and K_T the bulk modulus in GPa. Here we make the approximation that αK_T is constant with both V and T in the scanned domain, based on Ref. [28]. For KI, we use $\alpha K_T = 0.002$ GPa K^{-1}, in agreement with the values reported previously for KCl and KBr [28]; this represents a small thermal pressure of 2 GPa for a 1000 K temperature increase. The temperature of the PTM is assumed to be the average between the Sn-KI interface temperature measured with pyrometry and 300 K; the uncertainty in pressure due to the uncertainty in temperature is a few GPa.

Two ytterbium fiber lasers from the IPG Photonics company ($\lambda = 1070$ nm), which have a power stability of 1%, were focused on the sample from both sides. Once lasers were aligned, the laser power was increased steadily. The alignment between the x-ray beam and the heating spot was checked before and after each heating run with the PTM fluorescence induced by the x-ray beam. The fluorescence needs to be co-incident with the image of pinhole used to collect the thermal emission for temperature measurements through the optical chain.

During a ramp, XRD data were collected continuously with 5 s exposure time (PSICHE) and 1 s exposure time (ID27) resulting in up to hundreds of XRD patterns collected during one ramp. The bidimensional images were integrated using DIOPTAS software [32].

C. Temperature measurement

At PSICHE and ID27, temperatures were determined with both Planck and Wien fits on thermal emission data collected between 400–950 nm using reflective objectives (called "point pyrometry," PP, here) and a pinhole entrance to a spectrometer. The analyzed zone has a ∼3 μm diameter on the sample. The PP was performed upstream (side of incoming x rays) and downstream sides on PSICHE, and upstream side on ID27. Temperatures determined this way are expected to be reliable within ±100 to ±200 K for temperatures up to 4000 K, when collected thermal emission follows a Planck behavior [33].

At PSICHE, a new device (called "four color pyrometer" or "4C pyrometer" here) has been developed to map the temperatures over the sample, on upstream side. It is described in Ref. [34]. This device has been inspired by setups installed in laboratories [35,36]. A set of four images of the sample is recorded, each obtained in a narrow spectral range in the visible to near infrared with an individual optical path. This method is achromatic as each wavelength image is focused independently. Then, a region of interest is defined and the four images are correlated spatially in this region so that all emission maxima coincide; the output signal is a set of four intensity maps with typical size of 100×100 pixels, normalized by the reference spectrum of a calibrated lamp. Here, one pixel corresponds to 0.5 microns on the sample. For each pixel, the four normalized intensities are fitted with a Wien law. This produces a temperature map in the region of interest.

The number of point/4C pyrometry spectra was similar to the number of XRD data during a ramp.

III. ROOM TEMPERATURE COMPRESSION

A. EOS

Room temperature compression of tin was measured up to 223 GPa. Typical XRD patterns of the different phases are available in Ref. [25]. The $P - V$ points are plotted in Fig. 1 along with previous fit EOS reported in the literature [10,11] and tabulated data are provided in Ref. [25]. As expected, Sn undergoes several phase transformations that we monitored during pressure increase and decrease. Comparing our data with both non hydrostatic [11] and quasihydrostatic [9,10] conditions represents an opportunity to evaluate the effect of non hydrostatic compression on the sequence of phases measured on loading, and pressure-volume points.

Figure 1 shows the good agreement between P-V points collected under non hydrostatic (this work and Ref. [11]) and quasihydrotatic data (this work and Refs. [9,10]) below 100 GPa; which may be due to tin softness. We thus confirm the EOS parameters from Ref. [10] for β-Sn, bct-Sn, and bcc-Sn.

Data deviate between each other above 100 GPa, mostly in the hcp phase with a difference reaching $\Delta V / V = 1.6\%$ at 220 GPa. This corresponds to a pressure difference of 13 GPa. Salamat *et al.* [9] measurements reached 194 GPa, the pressure at which hcp Sn is just appearing in our experiments; a part of the discrepancy between our measured volumes may come from the extrapolation of their EOS at higher pressure. We suggest to use the following parameters for a Birch-Murnaghan EOS of hcp-Sn: $V_p = 13.8$ Å^3/at, K_p
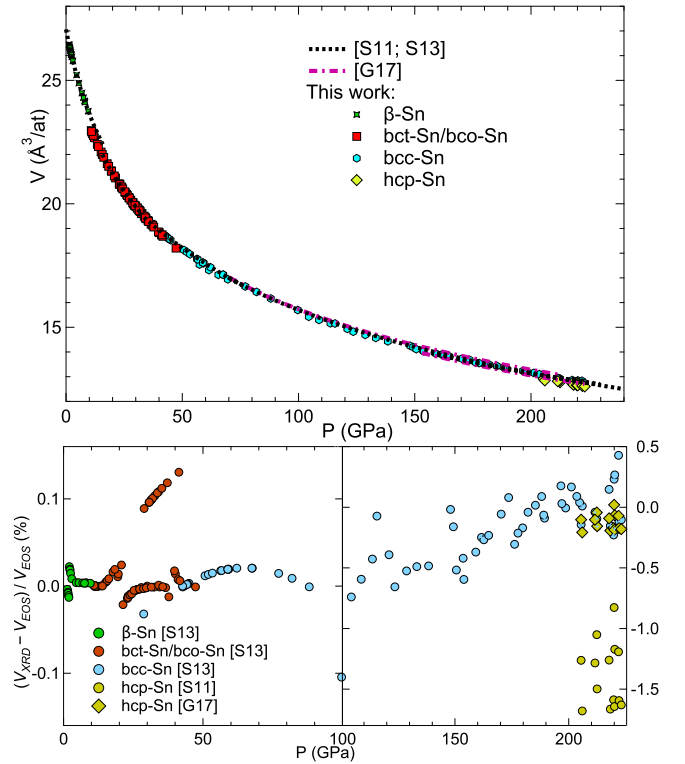

FIG. 1. Sn room temperature EoS. Pressure-volume points have been collected under nonhydrostatic compression above 15 GPa. The EOS from Refs. [9,10] (quasihydrostatic - black) and Ref. [11] (nonhydrostatic - red) are plotted as dashed lines. (Botton) Difference in percents between current and [9–11] EOS volumes. S11, S13, and G17 correspond to Refs. [9], [10], and [11], respectively.

= 652 GPa, and $K'_p = 5.1$ at 157 GPa; which is also in better agreement with Gavriliuk *et al.* data [11].

In a recent study, Bao *et al.* [37] predicted a new phase of tin under pressure with *ab initio* and DFT calculations. Phase (1) crystallises in space group $P2_1/m$, (2) is stable between 6.1 and 21.5 GPa, and (3) its transition with the β phase is accompanied by a volume drop of 2.4 %. This phase was not observed during our experiments.

B. β ↔ bct phase transition

Three compression-decompression cycles were performed during run Sn30 at 300 K and 425 K to measure β ↔ bct transitions conditions under hydrostatic compression [26].

Different single crystals of β-Sn had a starting state that could be distinguished from their XRD peaks: elongated by ±2° or by ±0.1° along the azimuthal direction (see inset of the Fig. 2). This elongation is related to dislocations density, and we call the crystals with large/small spread plastically strained/unstrained. For each crystal, the transitions proceed within one pressure step (which were of 0.4 GPa maximum), so that no coexistence domain could be detected as displayed in Fig. 2. Values of transition pressure are reported in Table II. Depending on the temperature and on the starting state, the pressure for the $\beta -$ Sn ↔ bct-Sn transitions differs: it is necessary to overshoot/undershoot the pressure for the direct/reverse transition for plastically unstrained crystals,
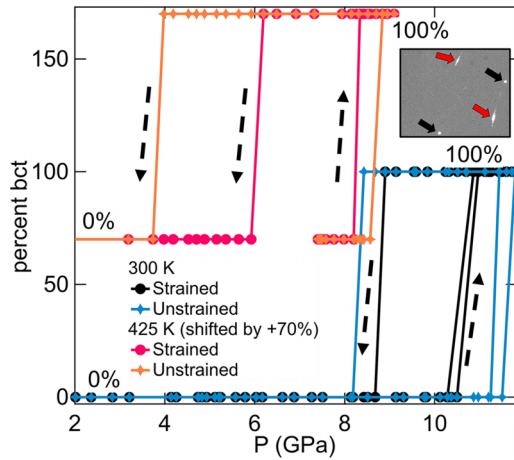
FIG. 2. Sn β-bct transition. Relative amount of bct-Sn measured during run Sn30. Dashed arrows identify compression-decompression cycles. (Inset) Diffraction spots for β-Sn at 4 GPa/300 K during run Sn30. Strained/unstrained crystals are shown with red/black arrows. For clarity, the data at 425 K have been shifted by 70%.

TABLE II. Pressures for the $\beta - \text{Sn} \leftrightarrow \text{bct-Sn}$ transitions during run Sn30 under hydrostatic conditions, with starting state (strained or unstrained). $\pm$ indicate maximum coexistence domains. Data from Refs. [10] (static hydrostatic loading) and [38] (shock loading) are included for comparison. TW: this work.

T (K)	Crystal	$P_{\beta \to \gamma}$ (GPa)	$P_{\gamma \to \beta}$ (GPa)	Ref.
300	unstrained	11.5 ± 0.1	8.3 ± 0.1	TW
	strained	10.7 ± 0.2	8.8 ± 0.1	TW
	unknown	13.2 ± 2.4		[10]
425	unstrained	8.7 ± 0.1	3.9 ± 0.2	TW
	strained	8.3 ± 0.1	6.1 ± 0.2	TW
~ 370	unknown	8.9 ± 0.5	7.1 ± 0.5	[38]

compared to plastically strained crystals. In Salamat *et al.* [10], a 5 GPa coexistence domain was reported under hydrostatic compression, which could originate from mixing of grains with different microstructures in the starting samples. The volume discontinuity of $\sim -1.9\%$ agrees with literature [10,38].

C. bct $\leftrightarrow$ bcc phase transition

A bct to bco transition has been previously observed at 32 GPa [10]. However, due to the similarity between the two phases ($c/a = 0.934$ and $a = b$ for bct-Sn, while $c/a = 0.937$ and $a/b = 0.996$ for bco-Sn), we were not able to discriminate these two phases: diffraction peaks collected under non hydrostatic compression can be either indexed with bco or

bct. Consequently, we decided to interpret all XRD data with bct-Sn when possible.

Figure 3 shows integrated XRD patterns evidencing the appearance/disappearance of bcc-Sn/bct-Sn on pressure increase. The relative amount of bcc-Sn, estimated using the intensity ratio between $(110)_{\text{bct}}$ and $(110)_{\text{bcc}}$ peaks, is also plotted. A pure bct-Sn phase is observed up to 36.6 ± 1.3 GPa. Around this pressure, the transition to a bcc structure begins. A domain of coexistence between the two phases is observed up to 57.1 ± 0.3 GPa (see Fig 3). Under quasi-hydrostatic compression, the transition begins/finishes at 41.2 GPa/70 GPa [10]. Non hydrostatic stresses thus reduce the pressure of the bct $\to$ bcc transition. Upon decompression, the reverse bcc to bct transition takes place from 31 GPa down to 16 GPa, evidencing a large hysteresis. From our data, taking the average of direct and reverse transitions, we estimate that the equilibrium pressure for bcc-bct transition in Sn is 34 ± 9 GPa.

D. bcc $\leftrightarrow$ hcp phase transition

In run Sn34, the diffraction peaks of hcp-Sn appear around 205 GPa, and a mixture of hcp-Sn and bcc-Sn is observed
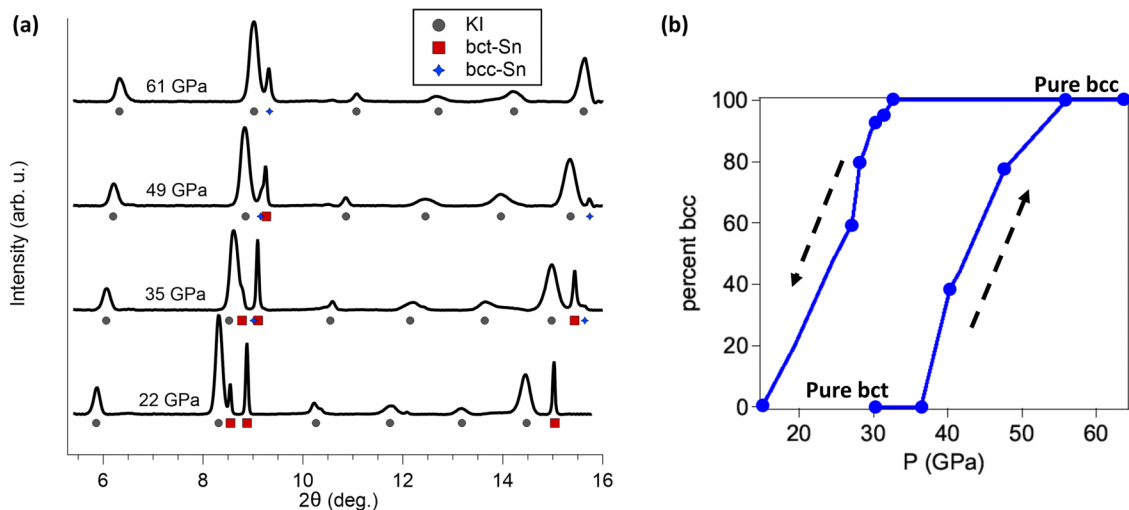

FIG. 3. Sn bct-bcc transition at 300 K. (a) XRD patterns for run Sn39. Red squares: bct-Sn, blue stars: bcc-Sn and gray disks: KI. (b) Relative amount of bcc-Sn measured for compression and decompression, estimated using the intensity ratio between $(110)_{\text{bct}}$ and $(110)_{\text{bcc}}$ peaks. Dashed arrows identify compression-decompression cycles.
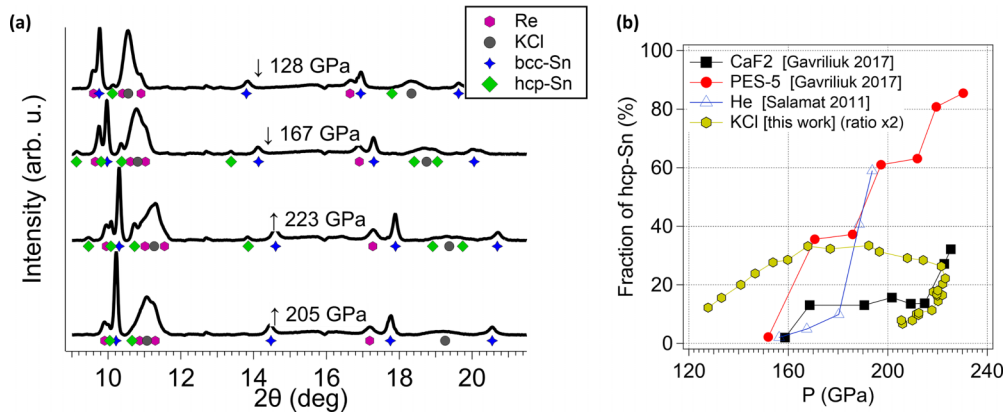
FIG. 4. Sn bcc-hcp transition at 300 K. (a) X-ray diffraction patterns collected during compression (↑)/decompression (↓) during run Sn34. Blue stars: bcc-Sn, green diamonds: hcp-Sn, gray circles: KCl and purple hexagons: Re. (b) Evolution of the fraction of hcp-Sn. For clarity, fraction of hcp-Sn was multiplied by 2 on the graph. Data from Refs. [9,11] are also plotted; pressure transmitting medium are indicated in the legend.

up to the maximum pressure reached, 225 GPa. The fraction of hcp-Sn estimated from the ratio between $(10\bar{1}0)_{hcp}$ and $(110)_{bcc}$ diffraction peaks intensities is plotted in Fig. 4(b) and x-ray diffraction patterns in Fig. 4(a). The bcc to hcp transition proceeds with a volume collapse of 1.5%, twice higher than measured in Ref. [9], and in agreement with Ref. [11]. Extrapolating the steady evolution measured, we estimate the pressure of 50% transformation: ∼240 GPa. During decompression, the decrease of XRD signal of hcp-Sn starts at 160 ± 5 GPa with a 50% transformation at ∼135 GPa [see Fig. 4(b)]. Our estimate of bcc-hcp equilibrium pressure at 300 K is thus $(135 + 240)/2 = 188$ GPa $\pm (-135 + 240)/2 = 53$ GPa.

Our study thus confirms the synthesis of hcp-Sn under high pressure at 300 K, but at higher pressure than previously reported [see Fig. 4(b)] [9,11]. Comparison between bcc-Sn volumes (Fig. 1) shows that the difference cannot be attributed to different pressure calibrations. DFT calculations predict that hcp and bcc phases a have similar energy (± 5 meV) in a large pressure range (from 100 to 200 GPa) [9,39]; with such a small difference, nonhydrostatic pressurization could shift the equilibrium pressure. The starting shape and microstructure (thin foil versus powder grains in Ref. [9]) may also have play a role in the transformation onset. Hcp-Sn was not observed by dynamic laser ramp compression experiments [13]: among other factors, high nonhydrostatic compression may have inhibited the transition in these experiments.

IV. HIGH-PRESSURE–HIGH-TEMPERATURE PHASE DIAGRAM

XRD data collected up to 110 GPa and 4000 K allow measuring solid phases stability domains as well as the melting curve of tin.

A. Point and 4C pyrometry

The precision of measured phase diagram depends in a large part on the accuracy of temperature measurements.

On ID27, the temperature was measured by a fit of thermal emission recorded on a 3×3 μm spot, on the upstream side

of the sample. A typical Wien fit is reported in Ref. [25]. The fit quality is good (0.2% residual) but one should keep in mind that temperature gradients can exist within the sample thickness.

On PSICHE, the temperature could be measured on the two sides of the sample, and laser power adapted in order to limit this gradient. 4C pyrometry measurements were carried out upstream.

Figures 5(a) and 5(b) present a comparison between pyrometry data collected upstream by the PP and 4C pyrometer, for one heating ramp. 4C temperatures measured on the location of the x-ray spot as well as the maximum temperatures are plotted. At the beginning of the heating ramp, the temperature is maximum on x-ray spot as the lasers had just been aligned on this location. 4C and pyrometer temperatures agree well within less than 100 K. Wien graphs plotted in Fig. 5(b) show that Wien functions are almost identical for PP and 4C at 09:45:38, and follow a linear trend as expected. With time, 4C x-ray and 4C maximum temperature progressively diverge, indicating that the heating spot deviates from x-ray spot. The temperature measured with the pyrometer also differs from 4C temperatures, reaching values up to ∼2000 K higher. Wien functions plotted in Fig. 5(b) show which signal is suitable: the 4C Wien function remains linear in the scanned wavelength range. We explain this by the truly achromatic character of the optical chain used for 4C pyrometer. On the other hand, the emission spectrum recorded by the PP pyrometer does not follow a linear behavior. A linear fit in the 1.3×10^6–1.6×10^6 m^{-1} domain overestimates temperature compared to 4C, and reducing the fitting domain only reduces this overestimate. A parasitic signal was probably collected due to aberrations, producing this apparent nongraybody behavior. As a matter of fact, after 09:49:00 4C pyrometer shows that thermal emission became very high, with a maximum temperature out of the pyrometry pinhole. 4C temperatures measured on X-ray spot location have thus been used, when available (see Table I).

Figure 5(c) shows the evolution of the hot spot for another heating ramp on the same sample: the hot spot expands and becomes double, which is likely due to a progressive
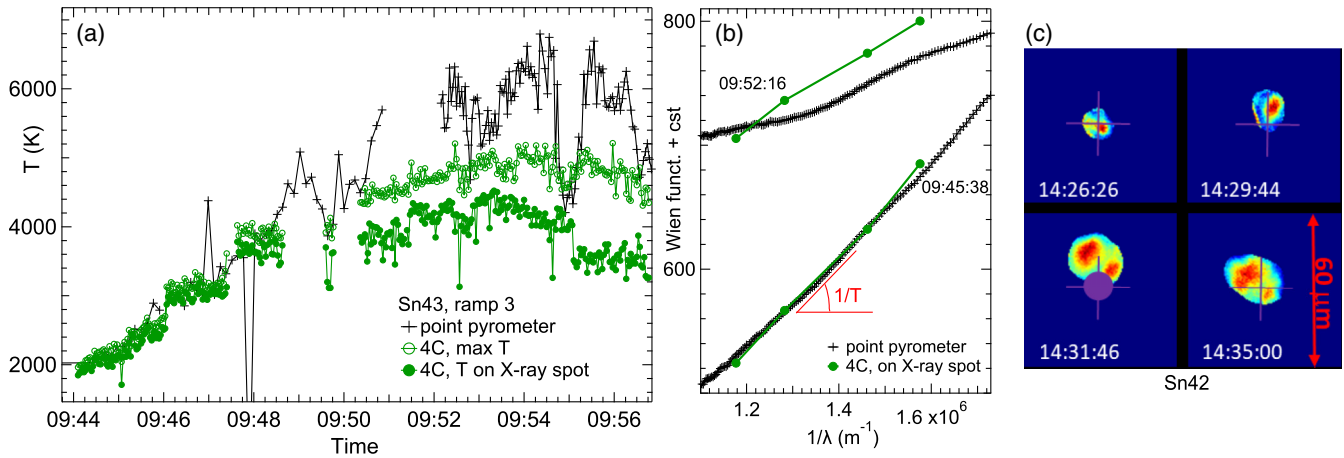
FIG. 5. Comparison between 4C point pyrometry and pyrometry data. (a) temperatures measured with point pyrometry and 4C pyrometry on the location of the x-ray spot for one heating ramp in run Sn34 at ~106 GPa. Maximum temperature is also plotted. (b) comparison between Wien fits for two different times during this ramp. (c) Temperature maps calculated by 4C pyrometer for another heating ramp. They show the progressive deviation of the maximum temperature from the x-ray location, indicated by the purple arrows and disk. The disk size is the approximate x-ray spot size on the sample.

misalignment of upstream and downstream lasers during the ramp. 4C pyrometery is useful to detect such unwanted situations, in real time, and to correct them by realigning the lasers.

B. bct ↔ bcc transition boundaries

The stability of the bct phase has been investigated under high temperature using laser heating experiments in the 300–1500 K and 20–60 GPa domain. Such temperatures are difficult to measure with pyrometry due to the low thermal emission signal. Below 1000 K, the temperatures were estimated from laser intensities and temperatures measured during the same ramp above 1000 K. Together with data reported in Ref. [15], the current data set enables to propose phase boundaries for the bct to bcc transition.

Integrated XRD patterns collected during a laser heating ramp at ~38 GPa are shown in Fig. 6(a). The (P,T) location of these spectra are indicated with black arrows on the phase diagram in the region of interest in Fig. 6(b). A bct → bcc (highest T) → bcc + bct → bct sequence is observed by heating → cooling of the sample. The bcc-phase is the only phase observed between 1300 K and melting. In a few runs, traces of metastable bcc-Sn could be observed after quench to 300 K, which disappeared on pressure change. This differs from the observation of the bct phase up to the melting point at 46 GPa in Ref. [20].

While heating and cooling cycles evidence an hysteresis for the bcc-bct transformation, as under ambient temperature and under isothermal compression at 600 K [15], it is impossible to disentangle this from the effect of unavoidable temperature gradients within the sample. We thus propose two
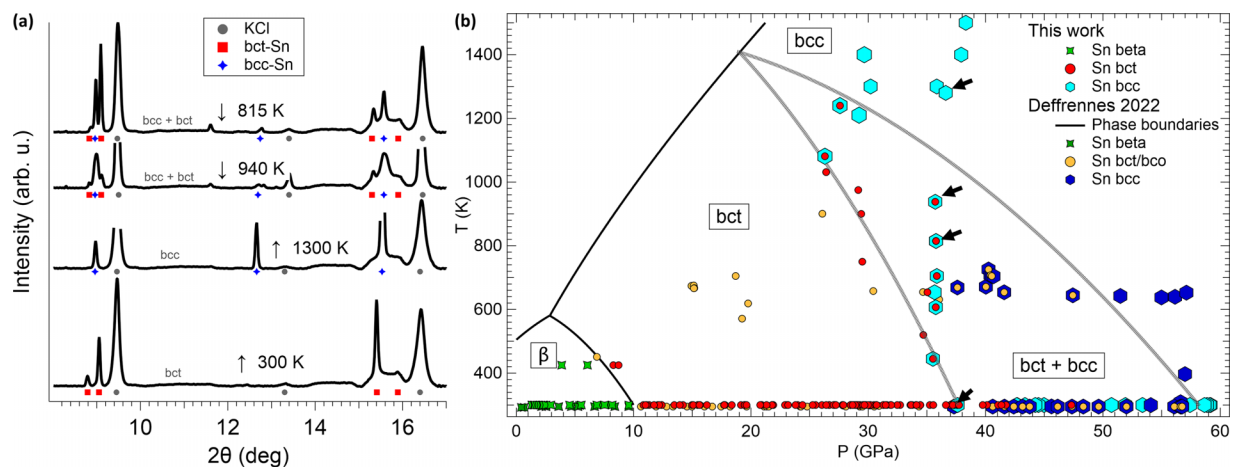

FIG. 6. Sn bcc-bct transition at HT. (a) Evolution of XRD patterns on *T* increase (↑)/decrease (↓) at ~38 GPa. Red squares: bct-Sn, blue stars: bcc-Sn and gray circles: KCl. (b) PT chart in the 0–60 GPa/300–1500 K range. Combined data from our experiments (laser heating) and from Ref. [15] (resistive heating). The two gray lines correspond to Eqs (2) and (3). Black arrows identify XRD patterns plotted in (a).
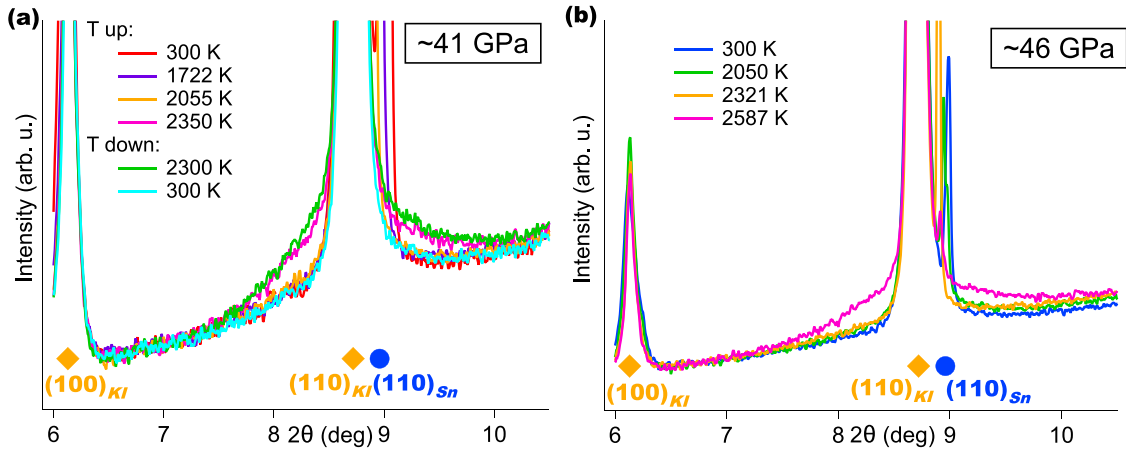
FIG. 7. Sn melting evidenced with x-ray diffraction. Stack of integrated XRD patterns collected during a laser heating ramp at (a) ~41 GPa in run Sn37 and (b) ~46 GPa in run Sn48.

boundaries based on our observations which are represented on a PT chart in Fig. 6(b). They separate PT conditions where: only a bct phase and a mixture of bct and bcc is observed (Eq. 2); only a bcc phase and a mixture of bct and bcc is observed [Eq. (3) - P in GPa, T in K]:

$$T = -1.07P^2 + 1.21P + 1771; \tag{2}$$

$$T = -0.43P^2 + 4.81P + 1472. \tag{3}$$

These boundaries cross the melting line at 18.9 GPa and 1410 K, close to liquid-bct-bcc triple point suggested by Deffrennes *et al.* [15] (20.4 GPa and 1566 K).

C. Melting of bcc-Sn

The first appearance of liquid scattering in the integrated XRD patterns is considered as the indicator of melting in diamond anvil cell samples [40–44]. Such signal, recorded mostly around (110) XRD peak of bcc-Sn, is presented in Fig. 7 for two heating ramps. Contrary to other metals [41–43], for which the liquid scattering x-ray signal can be recorded during a few minutes under continuous laser heating, we were able to evidence it during less than 10 s, despite numerous attempts. For this reason, only seven melting points could be unambiguously measured, and most of them at ESRF, where XRD collection time was shorter than at Soleil (1 s versus 5 s). For these points, the melting temperature is estimated as: $T_{\text{melt}} = (T_{\text{first liquid}} + T_{\text{last solid}})/2$, where $T_{\text{first liquid}}$ and $T_{\text{last solid}}$ are the lowest temperature of detection of a liquid diffuse signal, and the highest temperature of detection of a solid sample alone, respectively. Here, $T_{\text{last solid}}$ and $T_{\text{first liquid}}$ typically differ by 300 K, which results in an error of ± 150 K in the temperature of melting. These points are listed in Ref. [25]. The melting curve is thus constrained by (i) melting points at T_{melt} evidenced by appearance of diffuse signal; (ii) observation of the XRD signal of solid and unreacted bcc-Sn under high pressure/high temperature, which provides a lower bound for the melting curve.

Temperature runaways resulting in a damage of the sample were often observed after melting. There are two possible explanations for this behavior: a chemical reaction above melting point, or a change in optical properties of the sample at melting, resulting in an increased efficiency of laser heating. Below ~70 GPa, we did not detect any evidence of chemical reaction on the quenched sample XRD spectrum. The second interpretation is thus more likely, and in line with the observation of an increase of reflectivity after $\beta \to$ bct transition, followed by a decrease after melting during shock compression [45].

D. Chemical reaction with PTM

In runs Sn42, Sn43, and Sn46, reaching ~3000 K above 70 GPa resulted in a temperature runaway and in the formation of a new phase as evidenced on the XRD pattern of quenched sample (Fig. 8).

A fine (1×1 μm mesh) XRD mapping of the quenched sample on ID27 allowed finding the reacted zones and identifying the reaction product structure, even if this phase remained minor in the sample. The new phase has a face centered cubic (fcc) structure with a cell parameter $a = 4.178$ Å at 70 GPa. Its structure and cell parameter coincide with SnI_4 [46]. SnI_4 and pure I_2 EOSs are close, so that the exact stoichiometry of the product of reaction remains uncertain.

Between 70 GPa and 110 GPa, we observed a chemical reaction between Sn and KI only above Sn melting. Above 110 GPa, the reaction took place from the solid state in Sn. This is why no data collected above this pressure are presented in this report. Below we discuss only data points for which no evidence of a chemical reaction could be detected.

Briggs *et al.* performed melting experiments using KBr as PTM [20]. $SnBr_4$ also forms under high pressure [47] and without XRD diagnostic, which was not performed above 70 GPa in Ref. [20], a reaction between Sn and KBr cannot be ruled out.

E. Cross-check of measured temperatures with Sn EOS

To further check the validity of temperature measurements, we calculate V_{expected}, the expected volume of bcc-Sn at the pressure estimated using PTM XRD and EOS, and pyrometry temperature, and compare it with measured volume (Fig. 9).
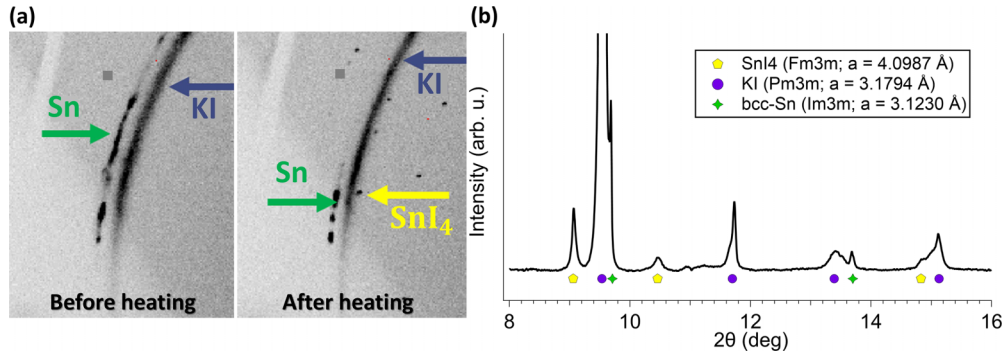
FIG. 8. Reaction between Sn and PTM during run Sn46. (a) XRD signal before and after laser heating at ∼90 GPa, showing the appearance of new XRD spots indicated in yellow. (b) Integrated XRD pattern showing SnI4 (lattice parameter $a = 4.099$ Å), Sn and KI after chemical reaction at 90 GPa.

V_{expected} is computed using Eq. (1), using $P(V, 300\text{ K})$ of bcc-Sn from Ref. [10] and $\alpha K_{\text{T Sn}} = 0.005$ GPa.K^{-1}, obtained by an analysis of Deffrennes *et al.* measurements [15]. Three examples are shown in Fig. 9.

In Fig. 9(a), a good correlation is found between the expected and measured volume below ∼2300 K. Then a sudden temperature jump is recorded; a faint XRD signal of a solid phase is still observed, which probably arises from cold zones scanned with the wings of the x-ray beam. For this ramp, temperature measurements are thus validated up to 2300 K. Expected and measured volumes agree in Fig. 9(b), and all measurements are validated up to the observation of the diffuse signal of molten Sn at 2715 K. In Fig. 9(c), the agreement is correct up to the highest temperature reached, ∼4200 K, where solid Sn is still observed. The differences between measured and expected volumes are all within 0.1 Å^3/at, which can be explained either by a systematic error in the equation of state of bcc-Sn, by uncertainties in temperature measurement and/or temperature variations of 300 K to 400 K (in the pressure range of 60–110 GPa). This order of magnitude corresponds to temperature differences within sample thickness or radius in the x-ray spot, estimated with finite elements modeling [48].

F. Phases of Sn under high PT

Figure 10 shows in a PT chart the phases of Sn measured for 10 different samples, for which 3 to 10 heating ramps validated by volume cross-check had been performed. For clarity, P/T errors bars were represented only for melting points corresponding to T_{melting} represented in pink. For those melting points, a conservative estimate is ±300 K, the sum of maximum pyrometry fitting error bars (±150 K) and ±150 K in the detection of melting (see Sec. IV C). Uncertainties in pressure are ± 3 GPa around 30 and 5 GPa at 110 GPa; they include the propagation of error bars in temperature of the PTM.

The melting points agree with earlier measurements [18,20] below 70 GPa. However, above 70 GPa, solid bcc-Sn is observed at temperatures above reported melting points measured by thermal analysis [20]. This could possibly been explained by a reaction between Sn and KBr PTM that would have biased this diagnostic. This reaction could have remained undetected as no XRD has been performed above 72 GPa in Ref. [20].

With the current data (melting points up to 65 GPa and solid points up to 110 GPa), we propose a lower bound for the melting curve under the form of a Simon equation (P in GPa,
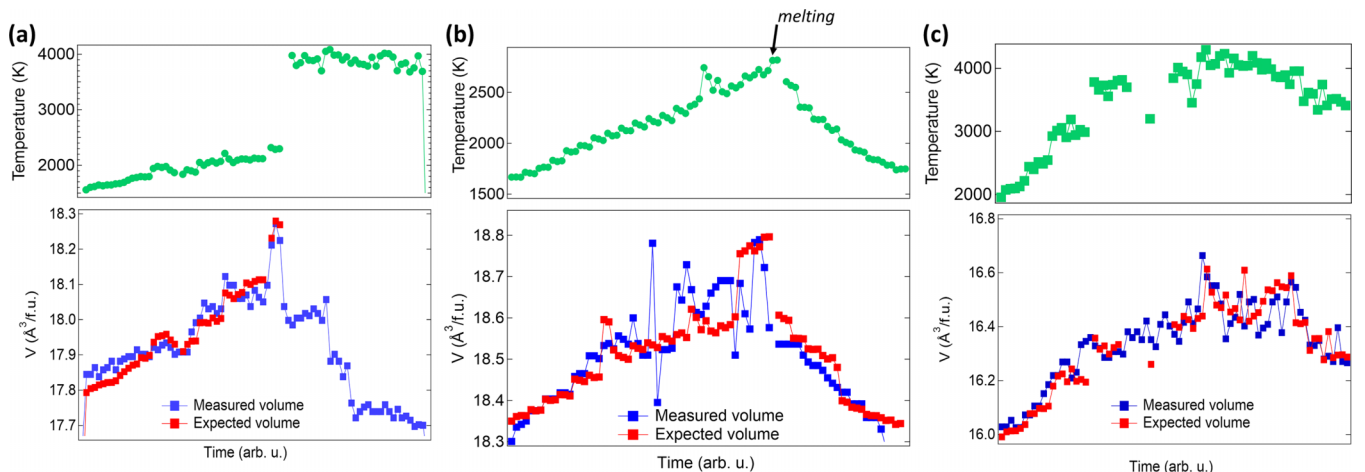

FIG. 9. Cross-calibration of our data during three heating ramps: (a) at ∼65 GPa, run Sn46. Temperature below 3000 K are validated. (b) at ∼55 GPa, run Sn47. A good agreement between calculated and experimental volume is observed. The black arrow shows time/temperature where diffuse scattering indicative of melting was observed. (c) At ∼100 GPa, run Sn43. This ramp is represented in Fig. 5.
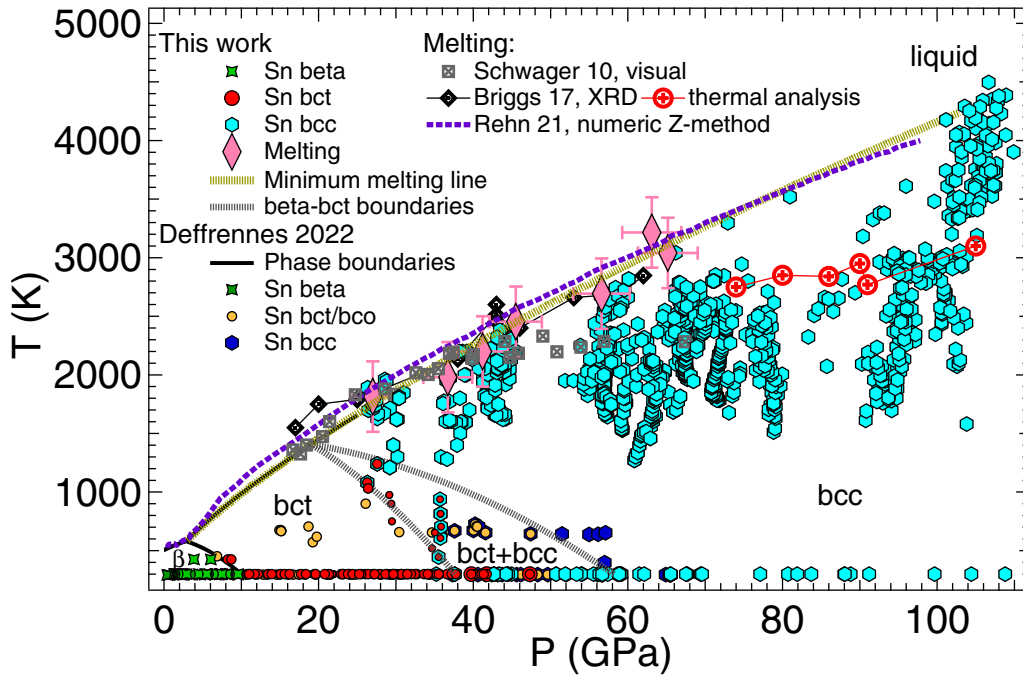
FIG. 10. Conditions where solid/liquid phases of Sn have been observed. Error bars are only presented for (P, T) points where liquid was observed to increase lisibility of the diagram. Data from literature [15,18,20,49] are added for direct comparison.

T_m in K):

$$T_m = 581 \left(\frac{P - 2.86}{6.44} + 1 \right)^{0.71}. \qquad (4)$$

Recently, Rehn *et al.* estimated the melting curve of bcc-Sn using ab initio molecular dynamics calculations with Z method [49]. They obtained a curve which agrees well with Eq. (4) as represented in Fig. 10.

V. CONCLUSION

The solid phases of tin have been investigated up to 225 GPa at room temperature. Pressures of both direct (on pressure increase) and reverse (on pressure decrease) transitions have been measured for β-bct, bct-bcc, and bcc-hcp transformations. All transitions exhibit a large hysteresis, the pressure difference between direct and reverse transitions being 2–4 GPa for β-bct, $\sim$20 GPa for bct-bcc, and $\sim$100 GPa for bcc-hcp. We observe that β-bct transitions conditions under hydrostatic compression are also strongly affected by the starting sample state (one grain plastically strained/unstrained), suggesting that plastic strain plays a role in the new phase nucleation. Similarly, the bcc-bct transition is favored by nonhydrostatic compression, but bcc-hcp transition seems to be rather inhibited by nonhydrostaticity. These observations illustrate the complex role of

pressurization conditions and microstructure in solid-solid phase transformations under static compression, and show the need to measure both (direct and reverse) transformations to constraint the equilibrium pressure.

High-pressure and high-temperature phase diagram of Sn has also been measured using x-ray diffraction in laser-heated diamond anvil cells up to 110 GPa and 4000 K. The stability field of the bcc phase is directly measured by the recording of its XRD signal in a dense (P,T) grid: it is wider than previously thought [20], with a higher melting curve above 70 GPa, and a lower bct $\rightarrow$ bcc transition temperature in the 30–50 GPa domain.

Tin and the alkali halide KI pressure medium start to react above 70 GPa in the liquid phase, producing likely SnI_4; the reaction is favored by further pressure increase and prevented high-temperature measurements above 110 GPa.

[1] C. A. Vanderborgh, Y. K. Vohra, H. Xia, and A. L. Ruoff, bcc lead at 109 GPa: Diffraction studies to 208 GPa, Phys. Rev. B **41**, 7338 (1990).

[2] M. I. McMahon, R. J. Nelmes, N. G. Wright, and D. R. Allan, Pressure dependence of the *Imma* phase of silicon, Phys. Rev. B **50**, 739 (1994).

[3] K. Takemura, U. Schwarz, K. Syassen, N. Christensen, M. Hanfland, D. Novikov, and I. Loa, High-pressure structures of Ge above 100 GPa, Phys. Status Solidi (b) **223**, 385 (2001).

[4] S. Gialanella, F. Deflorian, F. Girardi, I. Lonardelli, and S. Rossi, Kinetics and microstructural aspects of the allotropic transition in tin, J. Alloys Compd. **474**, 134 (2009).

[5] S. Desgreniers, Y. K. Vohra, and A. L. Ruoff, Tin at high pressure: An energy-dispersive x-ray-diffraction study to 120 GPa, Phys. Rev. B **39**, 10359 (1989).

[6] J. D. Barnett, V. E. Bean, and H. T. Hall, X-Ray diffraction studies on tin to 100 kilobars, J. Appl. Phys. **37**, 875 (1966).

[7] J. Hu, X. Zhou, C. Dai, H. Tan, and J. Li, Shock-induced bct-bcc transition and melting of tin identified by sound velocity measurements, J. Appl. Phys. **104**, 083520 (2008).

[8] L. Xu, Y. Bi, X. Li, Y. Wang, X. Cao, L. Cai, Z. Wang, and C. Meng, Phase diagram of tin determined by sound velocity measurements on multi-anvil apparatus up to 5 GPa and 800 K, J. Appl. Phys. **115**, 164903 (2014).

[9] A. Salamat, G. Garbarino, A. Dewaele, P. Bouvier, S. Petitgirard, C. J. Pickard, P. F. McMillan, and M. Mezouar, Dense close-packed phase of tin above 157 GPa observed experimentally via angle-dispersive x-ray diffraction, Phys. Rev. B **84**, 140104(R) (2011).

[10] A. Salamat, R. Briggs, P. Bouvier, S. Petitgirard, A. Dewaele, M. E. Cutler, F. Corà, D. Daisenberger, G. Garbarino, and P. F. McMillan, High-pressure structural transformations of Sn up to 138 GPa: Angle-dispersive synchrotron x-ray diffraction study, Phys. Rev. B **88**, 104104 (2013).

[11] A. G. Gavriliuk, I. A. Troyan, A. G. Ivanova, S. N. Aksenov, S. S. Starchikov, I. S. Lyubutin, W. Morgenroth, K. V. Glazyrin, and M. Mezouar, Structural transitions in elemental tin at ultra high pressures up to 230 GPa, JETP Lett. **106**, 733 (2017).

[12] N. A. Smirnov, *Ab initio* calculations of the phase diagrams of tin and lead under pressures up to a few TPa, J. Phys.: Condens. Matter **33**, 035402 (2021).

[13] A. Lazicki, J. R. Rygg, F. Coppari, R. Smith, D. Fratanduono, R. G. Kraus, G. W. Collins, R. Briggs, D. G. Braun, D. C. Swift, and J. H. Eggert, X-Ray diffraction of solid tin to 1.2 TPa, Phys. Rev. Lett. **115**, 075502 (2015).

[14] K. V. Khishchenko, Equation of state and phase diagram of tin at high pressures, J. Phys.: Conf. Ser. **121**, 022025 (2008).

[15] G. Deffrennes, P. Faure, F. Bottin, J.-M. Joubert, and B. Oudot, Tin (Sn) at high pressure: Review, X-ray diffraction, DFT calculations, and Gibbs energy modeling, J. Alloys Compd. **919**, 165675 (2022).

[16] C. Mabire and P. L. Héreil, Shock induced polymorphic transition and melting of tin, AIP Conf. Proc. **505**, 93 (2000).

[17] G. Robert, L. Pillon, G. Seisson, and C. Chauvin, Full multiphase description of materials: Application on tin, AIP Conf. Proc. **2272**, 070040, 2020).

[18] B. Schwager, M. Ross, S. Japel, and R. Boehler, Melting of Sn at high pressure: Comparisons with Pb, J. Chem. Phys. **133**, 084501 (2010).

[19] R. Briggs, D. Daisenberger, A. Salamat, G. Garbarino, M. Mezouar, M. Wilson, and P. F. McMillan, Melting of Sn to 1 Mbar, J. Phys.: Conf. Ser. **377**, 012035 (2012).

[20] R. Briggs, D. Daisenberger, O. T. Lord, A. Salamat, E. Bailey, M. J. Walter, and P. F. McMillan, High-pressure melting behavior of tin up to 105 GPa, Phys. Rev. B **95**, 054102 (2017).

[21] A. I. Golovashkin and G. P. Motulevich, Optical and electrical properties of tin, J. Exp. Theor. Phys. **46**, 460 (1964) [Sov. Phys. JETP **19**, 310 (1964)].

[22] R. Fréville, A. Dewaele, N. Guignot, G. Garbarino, and M. Mezouar, Equation of state of KI up to 150 GPa, High Press. Res. **43**, 251 (2023).

[23] S. Japel, B. Schwager, R. Boehler, and M. Ross, Melting of copper and nickel at high pressure: The role of *d* electrons, Phys. Rev. Lett. **95**, 167801 (2005).

[24] R. Freville, N. Bruzy, and A. Dewaele, Optical full-field strain measurement within a diamond anvil cell, Rev. Sci. Instrum. **94**, 123905 (2023).

[25] See Supplemental Material at http://link.aps.org/supplemental/10.1103/PhysRevB.109.104116 for the examples of sample loaded in a dac; xrd patterns during room compression, and a typical Wien fit to determine temperature.

[26] S. Klotz, J.-C. Chervin, P. Munsch, and G. Le Marchand, Hydrostatic limits of 11 pressure transmitting media, J. Phys. D: Appl. Phys. **42**, 075413 (2009).

[27] A. Dewaele and P. Loubeyre, Pressurizing conditions in helium-pressure-transmitting medium, High Press. Res. **27**, 419 (2007).

[28] A. Dewaele, A. B. Belonoshko, G. Garbarino, F. Occelli, P. Bouvier, M. Hanfland, and M. Mezouar, High-pressure–high-temperature equation of state of KCl and KBr, Phys. Rev. B **85**, 214105 (2012).

[29] P. I. Dorogokupets and A. Dewaele, Equations of state of MgO, au, pt, NaCl-B1, and NaCl-B2: Internally consistent high-temperature pressure scales, High Press. Res. **27**, 431 (2007).

[30] K. Takemura and A. Dewaele, Isothermal equation of state for gold with a He-pressure medium, Phys. Rev. B **78**, 104119 (2008).

[31] G. Shen, Y. Wang, A. Dewaele, C. Wu, D. E. Fratanduono, J. Eggert, S. Klotz, K. F. Dziubek, P. Loubeyre, O. V. Fat'yanov, P. D. Asimow, T. Mashimo, R. M. M. Wentzcovitch, and other members of the IPPS task group, Toward an international practical pressure scale: A proposal for an IPPS ruby gauge (IPPS-Ruby2020), High Press. Res. **40**, 299 (2020).

[32] C. Prescher and V. B. Prakapenka, DIOPTAS: A program for reduction of two-dimensional X-ray diffraction data and data exploration, High Press. Res. **35**, 223 (2015).

[33] L. R. Benedetti and P. Loubeyre, Temperature gradients, wavelength-dependent emissivity, and accuracy of high and very-high temperatures measured in the laser-heated diamond cell, High Press. Res. **24**, 423 (2004).

[34] N. Guignot, G. Morard, D. Antonangeli, S. Boccato, N. Jaisle, R. Pierru, L. Xie, P. Bouvier, J. Dominique, and J. Deslandes, Temperature mapping, beam shaping and indirect laser heating in diamond anvil cells on the PSICHE beamline, synchrotron SOLEIL, Acta Crystallogr. Sect. A **78**, e644 (2022).

[35] A. J. Campbell, Measurement of temperature distributions across laser heated samples by multispectral imaging radiometry, Rev. Sci. Instrum. **79**, 015108 (2008).

[36] O. T. Lord and W. Wang, MIRRORS: A MATLAB® GUI for temperature measurement by multispectral imaging radiometry, Rev. Sci. Instrum. **89**, 104903 (2018).

[37] X. Bao, H. Lang, X. Ma, T. Ou, M. Zhang, X. Zhang, and P. Li, New high-pressure monoclinic phase of Sn, Solid State Commun. **342**, 114635 (2022).

[38] R. Briggs, R. Torchio, A. Sollier, F. Occelli, L. Videau, N. Kretzschmar, and M. Wulff, Observation of the shock-induced β-Sn to b.c.t.-Sn transition using time-resolved X-ray diffraction, J. Synchrotron Radiat. **26**, 96 (2019).

[39] Y. Yao and D. D. Klug, Prediction of a bcc–hcp phase transition for Sn: A first-principles study, Solid State Commun. **151**, 1873 (2011).

[40] G. Shen, V. B. Prakapenka, M. L. Rivers, and S. R. Sutton, Structure of liquid iron at pressures up to 58 GPa, Phys. Rev. Lett. **92**, 185701 (2004).

[41] S. Anzellini, A. Dewaele, M. Mezouar, P. Loubeyre, and G. Morard, Melting of iron at earth's inner core boundary based on fast x-ray diffraction, Science **340**, 464 (2013).

[42] O. T. Lord, I. G. Wood, D. P. Dobson, L. Vočadlo, W. Wang, A. R. Thomson, E. T. Wann, G. Morard, M. Mezouar, and M. J. Walter, The melting curve of ni to 1 Mbar, Earth Planet. Sci. Lett. **408**, 226 (2014).

[43] S. Anzellini, D. Alfe, M. Pozzo, and D. Errandonea, Melting line of calcium characterized by in situ LH-DAC XRD and first-principles calculations, Sci. Rep. **11**, 15025 (2021).

[44] Y. Zhang, Y. Tan, H. Y. Geng, N. P. Salke, Z. Gao, J. Li, T. Sekine, Q. Wang, E. Greenberg, V. B. Prakapenka, and J.-F. Lin, Melting curve of vanadium up to 256 GPa: Consistency between experiments and theory, Phys. Rev. B **102**, 214104 (2020).

[45] B. M. La Lone, P. D. Asimow, O. V. Fat'yanov, R. S. Hixson, G. D. Stevens, W. D. Turley, and L. R. Veeser, High-pressure melt curve of shock-compressed tin measured using pyrometry and reflectance techniques, J. Appl. Phys. **126**, 225103 (2019).

[46] N. Hamaya, K. Sato, K. Usui-Watanabe, K. Fuchizaki, Y. Fujii, and Y. Ohishi, Amorphization and molecular dissociation of SnI_4 at high pressure, Phys. Rev. Lett. **79**, 4597 (1997).

[47] X. Huang, D. Duan, K. Wang, X. Yang, S. Jiang, W. Li, F. Li, Q. Zhou, X. Jin, B. Zou, B. Liu, and T. Cui, Structural and electronic changes of $SnBr_4$ under high pressure, J. Phys. Chem. C **117**, 8381 (2013).

[48] J. A. Montoya and A. F. Goncharov, Finite element calculations of the time dependent thermal fluxes in the laser-heated diamond anvil cell, J. Appl. Phys. **111**, 112617 (2012).

[49] D. A. Rehn, C. W. Greeff, L. Burakovsky, D. G. Sheppard, and S. D. Crockett, Multiphase tin equation of state using density functional theory, Phys. Rev. B **103**, 184102 (2021).